ACS Photonics

Article

pubs.acs.org/journal/apchd5

Wafer-Scale Aluminum Nanoplasmonic Resonators with Optimized Metal Deposition

Vladimir Liberman,*[,†] Kenneth Diest,[†] Corey W. Stull,[†] Matthew T. Cook,[†] Donna M. Lennon,[†] Mordechai Rothschild,[†] and Stefan Schoeche[‡]

[†]Lincoln Laboratory, Massachusetts Institute of Technology, Lexington, Massachusetts 02420, United States

[‡]J. A. Woollam Co., Inc., 645 M Street, Lincoln, Nebraska 68508, United States

Supporting Information

ABSTRACT: Spectroscopic ellipsometry is demonstrated to be an effective technique for assessing the quality of plasmonic resonances within aluminum nanostructures deposited with multiple techniques. The resonance quality of nanoplasmonic aluminum arrays is shown to be strongly dependent on the method of aluminum deposition. Three-layer metal−dielectric−metal nanopillar arrays were fabricated in a complementary metal-oxide semiconductor facility, with the arrays of nanopillars separated from a continuous metal underlayer by a thin dielectric spacer, to provide optimum field enhancement. Nanostructures patterned in optimized aluminum, which had been deposited with a high-temperature sputtering process followed by chemical mechanical planarization, display different resonance and depolarization behavior than nanostructures deposited by the more conventional evaporation process. Full plasmonic band diagrams are mapped over a wide range of incidence angles and wavelengths using spectroscopic ellipsometry and compared between aluminum nanostructures fabricated with two methods. The resonators fabricated from optimized aluminum exhibit a narrower bandwidth of both plasmonic resonance and depolarization parameters, indicating a higher quality resonance due to a stronger localization of the electric field. The optimized wafer-scale aluminum plasmonics fabrication should provide a pathway toward better quality devices for sensing and light detection in the ultraviolet and blue parts of the spectrum.

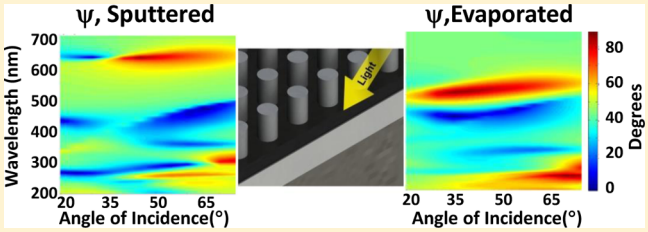

KEYWORDS: *localized plasmon resonance, Mueller-matrix spectroscopic ellipsometry, evaporated, sputtered, finite-difference time-domain*

The use of aluminum metal for ultraviolet plasmonics was first proposed almost 30 years ago.[1] Because the plasma frequency of aluminum is at significantly higher energies than that of gold or silver, aluminum holds promise for UV sensing and light-harvesting applications, with potential for enhanced line width narrowing, when compared with traditional plasmonic metals.[2] However, due to perceived deficiencies in the plasmonic response of aluminum via oxide formation and small grain sizes, aluminum plasmonics has only recently received significant attention. This resurgence of interest in aluminum plasmonics can be attributed to advances in deposition techniques and nanofabrication capabilities and improvement in material quality.[3−13] Applications of aluminum plasmonics are being pursued for energy harvesting and super absorbers,[14−20] sensing,[21−24] photodetection,[25,26] structural color,[27,28] holography,[29] and nanoantennae design.[30−40] Nevertheless, a robust underpinning of fabrication procedures, supported by advanced metrology, is still lacking and severely hinders the practical implementation of aluminum plasmonics.

Unlike plasmonic devices based on coinage metals, such as gold and silver, which are effectively banned from silicon semiconductor fabrication facilities, aluminum plasmonics can benefit from the vast infrastructure of complementary metal-oxide semiconductor (CMOS) technology, which is used for the fabrication of most of today's semiconductor chips. While a number of promising applications for aluminum plasmonics have been demonstrated, these studies have not taken advantage of wafer-scale plasmonic platforms, leveraging the compatibility of aluminum with CMOS infrastructure. Here, we demonstrate fully scalable aluminum plasmonics nanoresonator fabrication that utilizes the processing capabilities of semiconductor manufacturing, including sputtering, chemical mechanical polishing, atomic layer deposition, and reactively assisted ion etching. The design is based on metal−dielectric−metal multilayer structures, proposed for strong coupling of localized and propagating plasmon modes.[41] We show that aluminum nanostructures fabricated with an optimized aluminum process, based on high-temperature sputtering and planarization, have superior plasmonic properties when compared to the nanostructures produced by conventional evaporation.

Recently, spectroscopic Mueller-matrix ellipsometry has emerged as a powerful diagnostic for mapping of localized and propagating plasmon modes, characterization of fishnet

Received: December 27, 2015
Published: April 28, 2016

DOI: 10.1021/acsphotonics.5b00751
ACS Photonics 2016, 3, 796−805

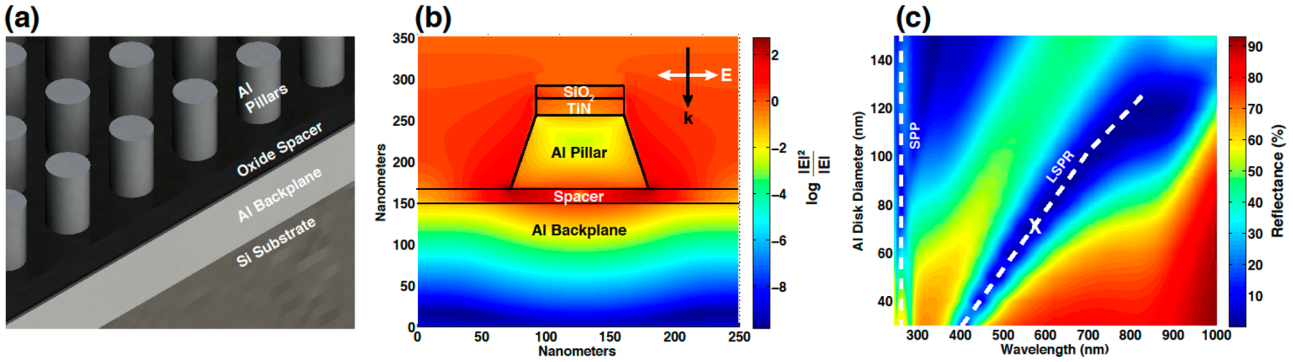

Figure 1. (a) Schematic of a plasmonic nanostructure stack, comprising Al pillars, separated by an aluminum oxide spacer from an Al backplane. Full-field simulation of an actual fabricated structure, showing electric field intensity distribution in cross-section, when irradiated at 575 nm at normal incidence. (c) Normal incidence reflectance map, showing a sweep of the top pillar dimension (labeled "diameter") and incident wavelength. The symbol "X" marking on the reflectance map corresponds to the geometry simulated in (b). Dashed lines indicate positions of the localized modes ("LSPR") and surface plasmon-polariton modes ("SPP"). (See text for further discussion and mode assignment.)

metamaterials, and assessment of quality factors of sharp resonances in photonic structures.[42−47] As compared to polarized reflectance measurements, ellipsometry offers several advantages: (a) measurements are highly accurate due to self-referencing; (b) phase information in addition to amplitude information is obtained; and (c) full polarimetry data are readily obtained through Mueller-matrix measurements. In this work, through the use of Mueller-matrix spectroscopic ellipsometry, we obtain a full plasmonic band diagram for the nanostructures. Furthermore, through the measurement of the ellipsometric depolarization parameter, we demonstrate a powerful connection between near-field plasmon localization and far-field light scattering.

RESULTS AND DISCUSSION

Nanoplasmonic Resonator Design. For the nanostructure design, we have chosen a three-layer periodic array of aluminum nanopillars spaced by a thin dielectric layer from a metallic mirror underlayer (Figure 1).[18,41,48,49] Coupling light into such structures excites both localized and propagating plasmon modes. Through the interference of these modes, perfect absorption and accompanying high local field intensities are expected at resonance wavelengths. Thus, such structures are useful for both sensing applications and the fundamental study of photon coupling into plasmonic modes.

We have modeled the three-layer nanoplasmonic array with full-field electromagnetic simulations (Figure 1). The layer schematic of the structure is shown in Figure 1a. The array pitch for this simulation is 250 nm. The calculated cross-section of the field distribution for a representative structure fabricated in this work is shown in Figure 1b under normal incidence irradiation. The taper of the pillar results from the dry etching process, as discussed below in the Wafer Scale Fabrication section. For this simulation, the aluminum oxide spacer layer thickness is 15 nm, the diameter of the top of the pillar is 75 nm, and the diameter of the bottom of the pillar is 95 nm. The thin SiO_2/TiN spacer layers on top of the pillar are needed for the dry etch mask, as described below. They are included in all the electromagnetic simulations; however, they do not impact the plasmonic resonances strongly. Strong enhancement of the electric field intensity is evident at the lower base of the pillar. While the resonance in the structure shown here occurs at 575 nm, the spectral position of the resonance and the strength of the resonance can be tailored by varying the diameter of the nanostructure and the thickness of the spacer layer. In fact, a recent publication shows a design for such an aluminum structure dimensionally optimized for UV excitation.[18] To demonstrate this wavelength tunability, we vary the top dimension of the nanopillar, keeping the aspect ratio constant (Figure 1c). We observe that a reflectance minimum can be tuned from 850 nm for the largest nanopillars down to <400 nm for nanopillar diameters under 40 nm. As will become evident in the discussion below, this tunable reflectance minimum arises from a localized surface plasmon resonance (LSPR). Additionally, a size-independent band below 250 nm can be observed at the lowest wavelengths of Figure 1c. As we discuss below, this band arises from a surface plasmon-polariton mode, which is not dependent on nanopillar size, but is dependent on the angle of incidence. Additional broader reflectance minima in Figure 1c arise for pillar diameters above 100 nm. These modes can be attributed to higher order resonances but are not observed for the structure dimensions of our work.

Wafer-Scale Fabrication. To access UV resonances in the nanoplasmonic structures, pillar diameters below 50 nm would be required (Figure 1c). Such feature sizes can be readily fabricated in current semiconductor fabrication facilities; however, they are on the same order as the grain structure of conventional electron-beam-evaporated aluminum films.[4] Due to preferential etching along metal grain boundaries, nanoscale structures from evaporated aluminum with feature sizes below 50 nm are incompatible with high-fidelity lithography and pattern transfer. To address the inadequacy of conventional room-temperature evaporation, we developed a wafer-scale aluminum deposition process, comprising high-temperature sputtering followed by chemical mechanical polishing (CMP), which resulted in micrometer-sized grains with subnanometer surface roughness. We have previously extensively characterized surface roughness, grain structure, and optical properties of such aluminum films. We also demonstrated that these films have a plasmonic figure of merit over 3 times higher than evaporated films throughout the visible and near-ultraviolet spectrum.[4]

In this work, we fabricated identical sets of nanopillar arrays on two separate wafers. The only difference between the two samples was the type of aluminum used: the first set of nanopillars was fabricated using aluminum deposited by high-temperature-sputtering/CMP, while the second set of nano-

DOI: 10.1021/acsphotonics.5b00751
ACS Photonics 2016, 3, 796−805

pillars was fabricated using aluminum deposited by electron beam evaporation. Simulations of Figure 1c suggest that near-UV-resonant structures can be obtained for pillar diameters less than 40 nm. However, for these smaller diameters, our "control" evaporated aluminum features would not survive the dry etching step due to their small grain size (50 nm size for evaporated Al vs 1400 nm for sputtered/CMP material[4]). Therefore, in this study the nominal diameter of the nanopillars for both types of aluminum was set at 75 nm, as defined using electron beam lithography. Hereafter, we refer to the first sample of aluminum arrays as "sputtered" and the second sample as "evaporated". For both samples, the pitch of the arrays was 250 nm, and the patterned area of the arrays was 9 mm^2. Cross-sectional diagram of the fabricated unit cell is shown in Figure 2. For both samples, the aluminum backplane is fabricated with a conventional unoptimized room-temperature sputtering process.

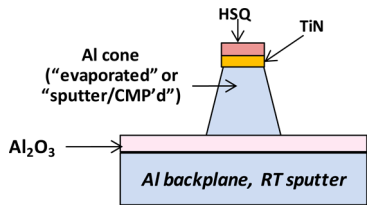

Figure 2. Cross-sectional diagram of a unit cell of a fabricated nanocone array.

The detailed fabrication process flow is described in the Methods section. All of the processes were developed in our silicon CMOS facility and are fully compatible with wafer-scale fabrication of transistors, imagers, and detectors.[50,51] In brief, a 20 nm thick titanium nitride layer was deposited between the top aluminum layer and the electron beam resist to protect the underlying aluminum during resist development. After lithography, the nanocone features were reactively ion etched with a Cl_2/BCl_3 mixture. Due to the dry etch used during patterning, the resultant structures had slightly tapered sidewalls, leading to a cone shape rather than vertical pillars (Figure 2, Figure 3a).

Cross-sectional scanning electron microscope images of the sputtered sample are shown in Figure 3a. The top of the nanopillars corresponds to the feature size defined by electron beam lithography, around 75 nm. The remainder of the hydrogen silsesquioxane (HSQ) electron beam resist layer and the titanium nitride layer is visible as a rounded protrusion near the top of the nanocone. The top-down SEMs show that the evaporated cone array (Figure 3b) has a higher density of defects, residue, and some cone asymmetry as compared to the sputtered array (Figure 3c), most likely resulting from preferential etching along the large number of grain boundaries present in evaporated aluminum metal.[4]

Optical Characterization. The subtle differences in geometry and array quality between the sputtered and the evaporated nanostructures (Figure 3b vs c) lead to large differences in optical response. The experimental normal reflectance spectra from the two arrays (Figure 4, dashed red lines) show two regions where minima occur: a deep resonance in the visible part of the spectrum that appears at 610 nm for the sputtered sample (Figure 4a) and at 500 nm for the evaporated sample, (Figure 4b) and multiple dips below 300 nm for both samples. The maximum reflectance level between the two dips near 400 nm reaches 70% in the sputtered sample, but only 55% in the evaporated sample, indicating the presence of additional absorption mechanisms in that region. These differences in optical signature are due to both the difference in material properties of the nanocones and changes in the cone dimensions and aspect ratio, as shown below. In order to properly interpret the optical response of our nanostructured arrays, we extracted average array dimensions using spectroscopic ellipsometric scatterometry.[52] In this technique, experimentally obtained ellipsometric data are matched against a computationally generated library of ellipsometric signatures for a number of variations of dimensional parameters. (Details of the extraction procedure are given in the Supporting Information.) Three parameters were varied to obtain agreement with the experimental data: height of the cones, base dimension of the cones, and the thickness of the dielectric spacer layer. Excellent agreement between the library data and the experimental data was obtained (Figure S2, Supporting Information). Using these extracted dimensions, the expected normal incidence reflectance was computed, utilizing the finite-difference time-domain (FDTD) technique. Excellent agreement between measured (dashed red traces, Figure 4a and b) and computed (solid blue traces, Figure 4a and b) responses

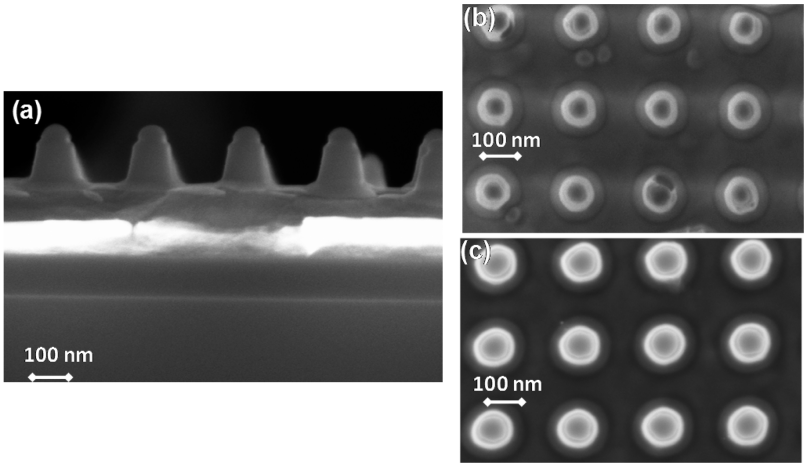

Figure 3. (a) Scanning electron micrograph (SEM) cross-section of sputtered aluminum nanocone samples. (b) Top-down SEM of evaporated aluminum sample. (c) Top-down SEM of sputtered aluminum sample.

DOI: 10.1021/acsphotonics.5b00751
ACS Photonics 2016, 3, 796−805

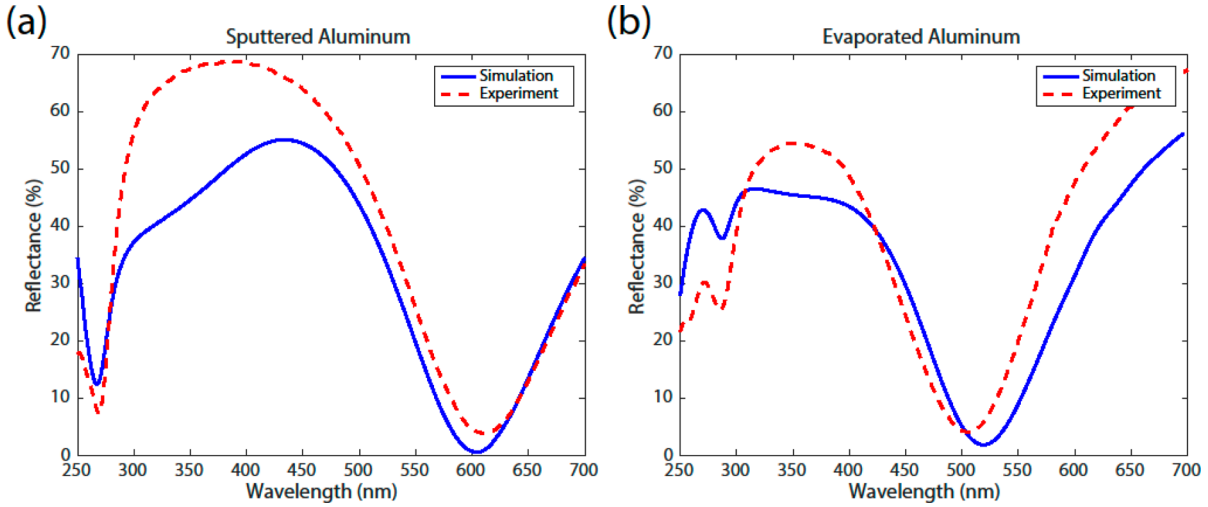

Figure 4. Normal incidence reflectance spectra from (a) the sputtered array and (b) the evaporated array. For each figure, experimental data are shown in dashed red and simulated results are shown in solid blue lines.

was obtained. From ellipsometric scatterometry, the extracted dielectric spacer thickness was 15 nm for the sputtered arrays and 18 nm for the evaporated arrays. For the evaporated array, the extracted base of the cone was 95 nm and the cone height was 100 nm, resulting in a sidewall slope angle of 85°. For the sputtered array, the extracted base of the cone was 115 nm and the cone height was 90 nm, leading to a sidewall slope angle of 77°. Such subtle changes in dimensions would be difficult to determine from electron micrograph inspection of Figure 3. Moreover, the optical measurements average structure dimensions over the ellipsometer spot size of ∼0.5 mm, corresponding to $>10^3$ periods. Such spatial averaging would not be possible with SEM imaging.

In order to assess the quality of plasmonics resonances and fully interpret the band structure, a more complete optical characterization is required in addition to normal incidence reflectance. For a broadband, broad-angle polarization-dependent analysis of the plasmonic resonances, we performed spectroscopic ellipsometry measurements of the two arrays (see Methods). The irradiation geometry and the angle of incidence for s- and p-polarizations are shown in Figure 5.

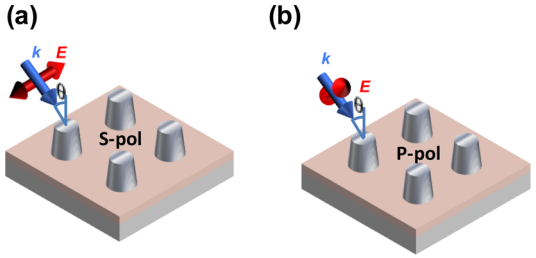

Figure 5. Geometry of the incident irradiation of the nanoplasmonic array: (a) s-polarization; (b) p-polarization.

Figure 6 compares previously shown reflectance data for the sputtered and evaporated arrays (Figure 6a and d, respectively) with the spectroscopic ellipsometry data for the same arrays (Figure 6b,c for sputtered and Figure 6e,f for the evaporated). The ellipsometric parameter Ψ represents the ratio of complex reflectances r_s and r_p at two polarizations, and Δ represents the phase between these two reflectances:

$$\rho = \frac{r_p}{r_s} = \tan(\psi)e^{i\Delta} \quad (1)$$

The data in Figure 6b and e are a representation of the plasmonic band diagram, as mapped out by spectroscopic ellipsometry. The wavelength vs angle-of-incidence (AOI) map could have been recast as the more conventional ω vs k diagram, but due to the uniform point density along the AOI axis, the representation in Figure 6 is more appropriate.[42] In eq 1, when the condition for the s-resonance is met, the magnitude of the right-hand side becomes large as Ψ tends to 90°. Thus, bright red colors in Figure 6b and e represent s-resonances. Analogously, dark blue colors in Figure 6b and e represent p-resonances. As observed by others, the location of these plasmonic resonances is accompanied by a sharp change in phase (Figure 6c and f).[53]

To understand the nature of the resonances, we use the extracted structure dimensions for evaporated and sputtered samples (see Supporting Information, Table S1) to perform full-field FDTD simulations at oblique angles of incidence. Figure 7 shows the computed p-polarized (Figure 7a) and s-polarized (Figure 7b) reflectances for sputtered (red traces) and evaporated (blue traces) samples, all at a 65° angle of incidence. We notice an excellent correspondence between the predicted resonance positions at 65° of Figure 7 and experimental resonances of Figure 6b and e. (The resonance widths are not fully captured by the simulations, since these are influenced by differences in metal grain sizes and surface roughness, which are not explicitly modeled.) The wavelength positions of certain resonances appear to vary for evaporated vs sputtered samples, such as s-polarized resonances between 550 and 600 nm (Figure 7b). On the other hand, wavelength positions of other resonances appear to be sample-independent, such as p-polarized resonances at 480 and ∼200 nm and s-polarized resonance near 250 nm.

We identify the resonances with a sample-dependent wavelength position between 500 and 600 nm as localized plasmonic modes. To understand the near-field mode profile, we compute the electric field intensity for the sputtered sample in the vertical plane at normal AOI and 600 nm incident wavelength (Figure 8a). Here, the incident polarization vector is in the plane of the figure, analogously with the irradiation

DOI: 10.1021/acsphotonics.5b00751
ACS Photonics 2016, 3, 796−805

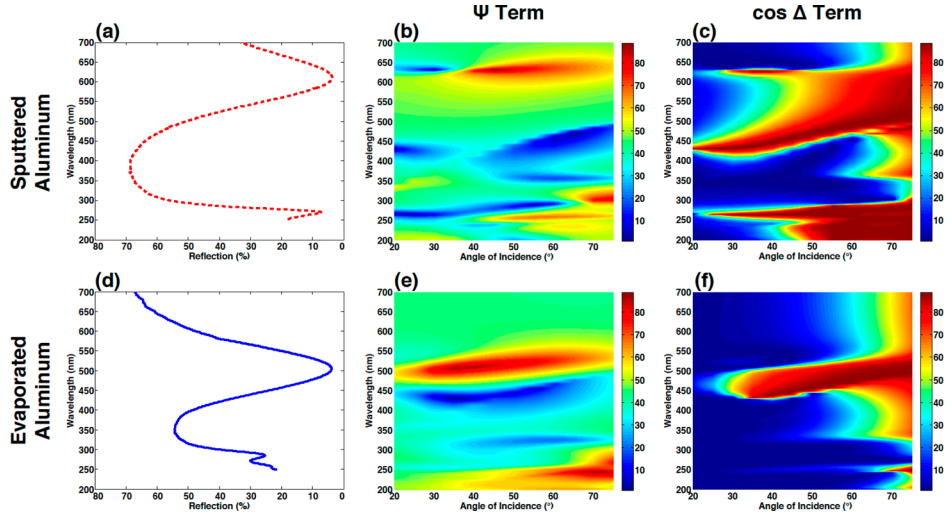

Figure 6. Normal-incidence reflectance, Ψ ellipsometric parameter, and cos(Δ) ellipsometric paramater for sputtered samples (a, b, and c, respectively) and evaporated samples (d, e, and f, respectively).

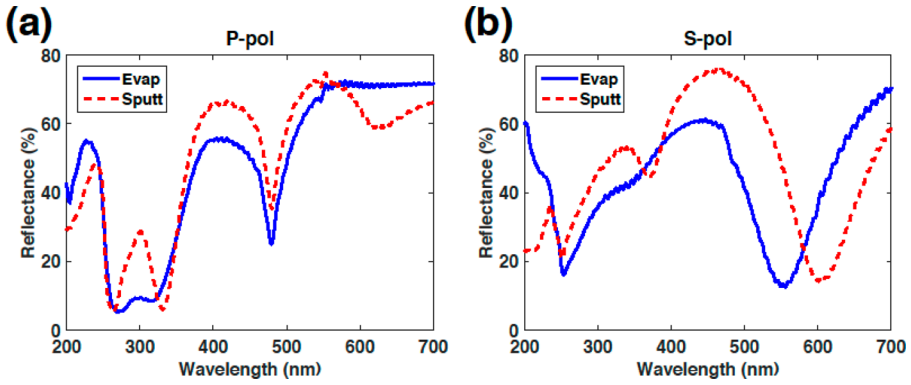

Figure 7. Computed reflectances for 65° angle of incidence: (a) p-polarized reflectance and (b) s-polarized reflectance. Blue traces refer to evaporated samples, and red traces refer to the sputtered samples.

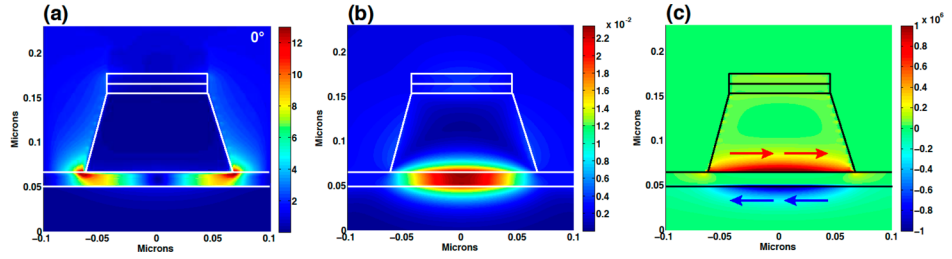

Figure 8. Computed near-field profiles in the vertical plane for the sputtered Al array at normal incidence, 600 nm wavelength resonance. Structure outlines are shown. (a) *E*-field intensity. (b) Out-of-plane *H* field. (c) Horizontal current density *J*.

geometry of Figure 1b. The electric field distribution for these localized modes is strongly confined at the lower edge of the aluminum cones and, thus, is highly sensitive to material losses. This excitation can be recognized as a magnetic dipole resonance, which arises from the coupling between the bottom of the plasmonic pillar and the top of the metal underlayer to form a localized current loop.[54] (See Figure 8b and c.)

We observe a much sharper LSP resonance in the sputtered sample vs evaporated sample, by comparing the red resonance region in Figure 6b near 600 nm vs the corresponding red resonance region in Figure 6e near 550 nm. This difference is highlighted by plotting the Ψ parameter as a function of wavelength for a 45° angle of incidence (Figure 9). The quality factors of the LSPR in the two samples are computed by dividing the peak position by the full width at half-maximum (fwhm) of the Ψ parameter, in accordance with methodology of a recent ellipsometric study.[45] The quality factor for the sputtered sample is 3 times higher than that for the evaporated sample. The narrower plasmonic line width of the LSP resonance for the sputtered sample can be due to at least two reasons. First, since the wavelength of the LSPR is sensitive to cone dimensions, better uniformity of the sputtered Al plasmonic cones (Figure 3b vs c) can lead to narrower line widths. Second, higher quality sputtered aluminum due to its larger grain size and, thus, reduced scattering leads to a higher quality factor of the resonance and a sharper peak.

DOI: 10.1021/acsphotonics.5b00751
ACS Photonics 2016, 3, 796−805

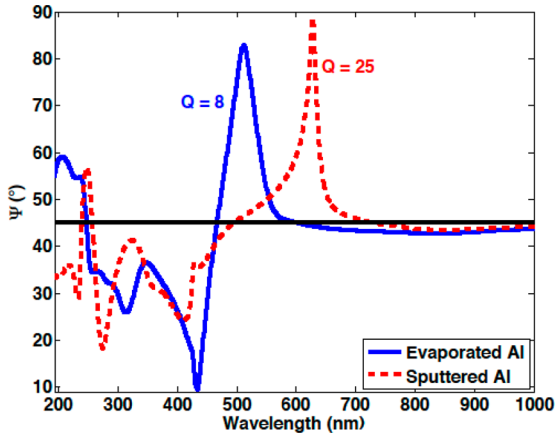

Figure 9. Ellipsometric Ψ parameter vs wavelength for 45° AOI for evaporated (solid blue) and sputtered (dashed red) samples. Quality factors of the resonance are shown next to each peak.

It is instructive to note that, although oblique angle-of-incidence data show a substantial difference between the widths of the plasmonic resonance (Figure 6b vs e), the normal-incidence data for the two arrays show comparable line widths (Figure 6a vs d). The difference between the normal-incidence and the oblique-incidence data is investigated by examination of near-field profiles for 0° vs 45° angle of incidence at 620 nm (Figure 10). At 45° AOI, the electric field intensity is highly localized at the edge of the nanocones (Figure 10a), whereas at normal incidence, the interaction with the aluminum underlayer is considerably greater (Figure 10b). Since for both our structures the aluminum underlayer is prepared from unoptimized aluminum, resonance broadening at 0° over 45° incidence angle can be expected due to larger losses from the aluminum underlayer.[4] Thus, the oblique angle-of-incidence data represent a more accurate assessment of the plasmonic resonance quality in the nanocones.

The central message of this study is to demonstrate the effect of material deposition on the quality of plasmonic modes, which is best demonstrated for LSPR resonances, discussed above. However, for completeness, we analyze the rest of the modes in the plasmonic band diagram of Figure 6. Assignment of these modes is complicated by the cone taper in the structure and the strong coupling between various modes. As in the discussion of Figure 7, we identify the propagating modes as those independent of pillar size, and the localized modes as those occurring at different wavelengths for sputtered vs evaporated samples due to differences in pillar dimensions. Thus, p-polarized band between 45° and 70° AOI at 350 nm in the sputtered sample and at 320 nm in the evaporated sample (Figure 6b and e) is due to the higher order (quadrupolar) resonance localized at the bottom of the structure, as confirmed by FDTD simulations. On the other hand, the strong p-polarized mode that occurs in both samples at 65° near 470 nm but shifts downward in wavelength with an angle of incidence can be assigned to a (−1,0) SPP mode from the dispersion curve, predicted by the grating equations (see Supporting Information, Figure S3). The 240 nm s-polarized excitation at 65° AOI (see Figure 7b) corresponds to the (−1,1) SPP mode. (Note that due to our square array geometry, both p-polarization and s-polarization excitation of the SPP modes is possible.[55]) The field profile for this SPP mode is shown in the Supporting information, Figure S4. The strong p-band observed between 250 and 300 nm (Figure 6b) is a mixture of a localized resonance and a gap mode (see discussion below and Figure 12).

As a final part of the study, we have extracted the depolarization parameter from the ellipsometric data acquired along the high-symmetry directions. For isotropic samples, depolarization can be described as a mixture of a non-depolarizing matrix and an ideal depolarizer. The degree of polarization, p, is extracted from the isotropic ellipsometry parameters, N, C, and S,[56] where

$$p = \sqrt{N^2 + C^2 + S^2} \tag{2}$$

In the above, $N = \cos(2\Psi)$, $S = \sin(2\Psi)\sin(\Delta)$, and $C = \sin(2\Psi)\cos(\Delta)$, where Ψ and Δ are the traditional ellipsometry angles. The % depolarization is then defined as

$$\%\text{depol} = 100 \times (1 - p^2) \tag{3}$$

In our case, the high-symmetry array directions were identified by performing azimuthal in-plane scans and identifying the angles where the off-diagonal Mueller-matrix elements were minimized (see Methods).

The highest depolarization for either sample (Figure 11) occurs at the spectral position of the main plasmonic resonances (see Figure 6), where depolarization for both samples reaches nearly 70%. By contrast, no depolarization is observed in the spectral regions away from plasmonic resonances. The spectral bandwidth of maximum depolarization for the evaporated sample is much broader than that of the sputtered sample.

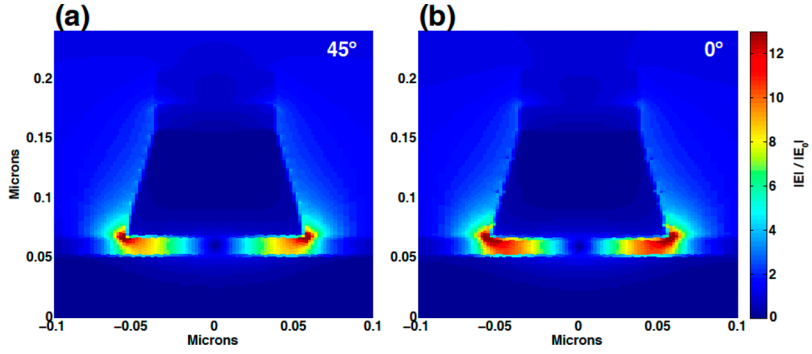

Figure 10. Cross-section field profiles for the sputtered aluminum sample at 45° incident angle (a) and 0° incident angle and (b) at 620 nm and for s-polarized light, shown in the plane of polarization.

DOI: 10.1021/acsphotonics.5b00751
ACS Photonics 2016, 3, 796−805

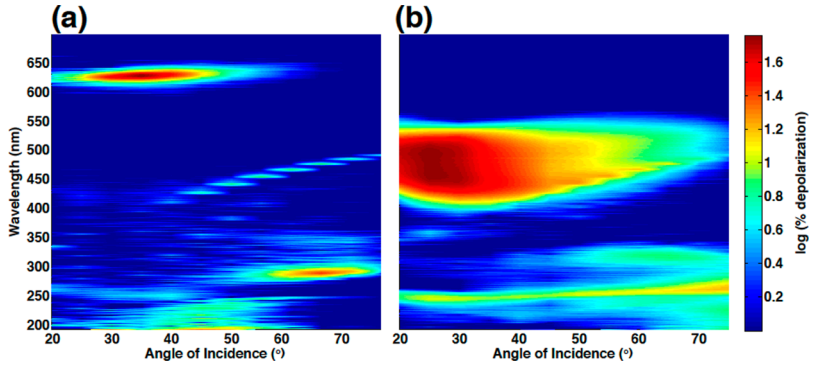

Figure 11. Ellipsometrically acquired spectral depolarization map for the sputtered sample (a) and evaporated sample (b).

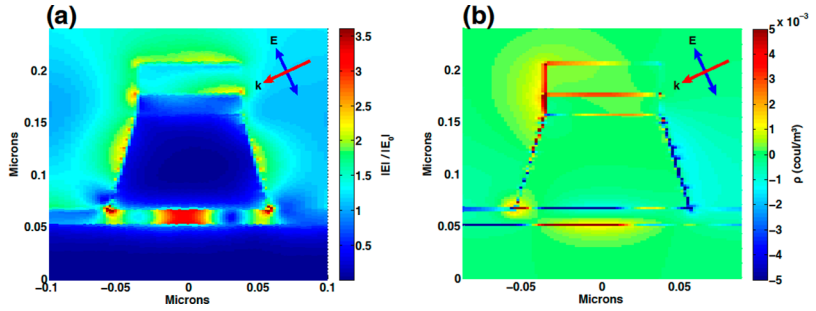

Figure 12. Cross-sectional field profile (a) and charge density (b) for the sputtered sample, calculated from full-field simulations at 65° angle of incidence and 265 nm wavelength. The upper-right inset on each plot shows the geometry of the incident *k*-vector and the electric field.

Previous work on diffractively coupled plasmonic dimer arrays similarly measured the spectral regions of maximum depolarization utilizing spectroscopic ellipsometry.[57] That work demonstrated that maximum depolarization occurred in the regions of the maximum electric field enhancement. The authors postulated that depolarization arose due to the finite detector size, which was able to capture a finite range of diffracted wavevectors, each characterized by a well-defined polarization state. In the vicinity of the plasmonic resonances, the higher spatial near-field localization directly translated to the increased depolarization in the far field due to the larger angular spread of the wavevectors.

In this work, we further suggest that the narrow spectral bandwidth of the depolarization for the sputtered sample arises from the higher resonance quality of that sample. By comparison, the broader spectral bandwidth of the depolarization for the evaporated sample arises from the broader spectral width of that resonance (Figure 6e).

It is also interesting to observe a second, high-depolarization region occurring in both samples at higher angles of incidence between 250 and 300 nm. Near-field and charge density simulations for this mode suggest strong field localization at the bottom of the structure, with additional coupling across the dielectric gap into a gap mode in the underlying metal (see Figure 12a and b). Once again, we suggest that the strong near field localization is observed in the far field as an increase in the depolarization parameter.

CONCLUSIONS

We have developed a robust, wafer-scale fabrication method for aluminum nanoplasmonic structures for ultraviolet and visible applications. Two sets of structures, utilizing conventional evaporated aluminum and improved high-temperature-sputtered-and-polished aluminum, were fabricated and characterized utilizing spectroscopic ellipsometry. The differences in thin-film processing lead to different grain structure and slightly different nanostructure dimensions. Although these differences appear to be small as observed by conventional scanning electron beam imaging, they nevertheless have a profound effect on the near-field and far-field optical behavior of plasmonic resonators. Significantly higher quality resonances were demonstrated for the nanostructures fabricated using the improved aluminum deposition process. Furthermore, depolarization data obtained with spectroscopic ellipsometry suggests that structures fabricated in the improved aluminum exhibit better near-field spatial localization when compared with evaporated aluminum films. This fabrication demonstration provides a robust platform for CMOS-compatible, wafer-scale plasmonic devices that enable a range of efficient sensing and light-harvesting applications in the ultraviolet-to-visible wavelength range.

METHODS

Simulations. For dimensional extractions utilizing the ellipsometric scatterometry method, rigorously coupled wave analysis software Unigit was used (see Supporting Information).[58] For full-field electromagnetic simulations, finite-difference time-domain method software FDTD Solutions from Lumerical Corporation was used.[59]

Spectroscopic Ellipsometry Measurements. The data were acquired using a dual-rotating compensator ellipsometer (J.A. Woollam RC2) over the wavelength range from 193 to 1690 nm at angles of incidence between 20° and 75° in steps of 5°. The sample was mounted on an automated rotation stage, and data were acquired for azimuthal orientations between 0° and 360° in increments of 7.5°. Focusing probes were used to reduce the beam diameter at the measurement spot to approximately 250 μm. The entire 4 × 4 Mueller-matrix data

DOI: 10.1021/acsphotonics.5b00751
ACS Photonics 2016, 3, 796−805

normalized by the element M_{11} were obtained at the above experimental conditions. For the analysis in this paper, only the data along the high-symmetry directions are presented.

Fabrication of Nanopillar Arrays. To fabricate both samples, 8 in. diameter (100) silicon was used as the starting substrate. The first layer in both samples was 200 nm thick aluminum deposited using dc magnetron sputtering in an argon−hydrogen environment. The deposition power was 1 kW, the Ar flow rate was 10 sccm, and the 90%:10% Ar:H flow rate was 15 sccm. There was no active control of the substrate temperature, and the film thickness was verified using spreading sheet resistance. The second layer in both samples was 20 nm thick aluminum oxide deposited using atomic layer deposition. For both samples, the oxide was thermally deposited at 300 °C using trimethylaluminum and deionized water. The film thickness was verified using spectroscopic ellipsometry.

The third layer was the only layer that was different between the two samples. The first sample had a 500 nm thick aluminum film deposited on the aluminum oxide layer using dc magnetron sputtering in an argon environment. The deposition power was 2 kW, the Ar flow rate was 50 sccm, and the chamber pressure was 6 mTorr. The substrate was kept at 350 °C during deposition, and the film thickness was verified using spreading sheet resistance. This was followed by a chemical mechanical polishing step to thin the aluminum to ∼130 nm. The combination of high deposition temperature and CMP was used to produce an aluminum film with both large grain size and low surface roughness.[4] The second sample had a ∼130 nm thick aluminum film deposited on the aluminum oxide layer using electron beam evaporation with no active control of the substrate temperature at a base pressure of 9.5×10^{-9} Torr and a deposition rate of 0.5 Å/s.

The fourth layer in both samples was 20 nm thick titanium nitride deposited using dc magnetron sputtering in an argon−nitrogen environment. The deposition power was 12 kW, the Ar flow rate was 20 sccm, and the N_2 flow rate was 70 sccm. The substrate was kept at 150 °C during deposition, and the film thickness was verified using spreading sheet resistance.

Both samples were then patterned using electron beam lithography at 100 kV accelerating voltage. Hexamethyldisilazane (HMDS) was first used to pretreat the surface of the samples before spin coating with hydrogen silsesquioxane resist.[60] HSQ is a spin-on glass, with excellent etch resistance and resolution, that has been used extensively in electron beam lithography over the past two decades. A 3 mm × 3 mm area was patterned with a square array of circles, which was written with a 250 nm pitch and a 70 nm diameter. The resist was exposed with a dose of 3200 $\mu C/cm^2$ and was developed for 120 s at room temperature in MF-26A (Rohm and Haas Electronic Materials), which is an ammonium hydroxide-based developer. Finally, samples were plasma etched using a 1200 W plasma with a 145 W bias and a 12 mTorr chamber pressure. The flow rates for the chlorine, boron trichloride, nitrogen, and argon were 100, 40, 20, and 100 sccm, respectively. *In-situ* end-point detection was used to stop each etch once the top aluminum layer was removed.

Finally, we should note that the 20 nm thick titanium nitride layer was not added for any optical purpose. This layer served as a protective coating between the underlying aluminum and the ammonium hydroxide used to develop the HSQ resist. Samples fabricated without this layer were destroyed during the resist development step.

■ ASSOCIATED CONTENT

Supporting Information

The Supporting Information is available free of charge on the ACS Publications website at DOI: 10.1021/acsphotonics.5b00751.

Critical dimension extraction with ellipsometric scatterometry, SPP dispersion calculation, and SPP near-field profiles (PDF)

■ AUTHOR INFORMATION

Corresponding Author

*E-mail (V. Liberman): vlad@ll.mit.edu.

Notes

The authors declare no competing financial interest.

■ ACKNOWLEDGMENTS

The Lincoln Laboratory portion of this work was sponsored by Assistant Secretary of Defense for Research & Engineering under Air Force Contract #FA8721-05-C-0002. Opinions, interpretations, conclusions, and recommendations are those of the authors and do not necessarily represent the view of the United States Government.

■ REFERENCES

(1) Zeman, E. J.; Schatz, G. C. An accurate electromagnetic theory study of surface enhancement factors for Ag, Au, Cu, Li, Na, Al, Ga, In, Zn, and Cd. *J. Phys. Chem.* **1987**, *91*, 634−43.

(2) Sobhani, A.; Manjavacas, A.; Cao, Y.; McClain, M. J.; García de Abajo, F. J.; Nordlander, P.; Halas, N. J. Pronounced Linewidth Narrowing of an Aluminum Nanoparticle Plasmon Resonance by Interaction with an Aluminum Metallic Film. *Nano Lett.* **2015**, *15*, 6946−6951.

(3) Taguchi, A.; Saito, Y.; Watanabe, K.; Yijian, S.; Kawata, S. Tailoring plasmon resonances in the deep-ultraviolet by size-tunable fabrication of aluminum nanostructures. *Appl. Phys. Lett.* **2012**, *101*, 101.

(4) Diest, K.; Liberman, V.; Lennon, D. M.; Welander, P. B.; Rothschild, M. Aluminum plasmonics: Optimization of plasmonic properties using liquid-prism-coupled ellipsometry. *Opt. Express* **2013**, *21*, 28638−28650.

(5) Maidecchi, G.; Gonella, G.; Proietti Zaccaria, R.; Moroni, R.; Anghinolfi, L.; Giglia, A.; Nannarone, S.; Mattera, L.; Dai, H.-L.; Canepa, M.; Bisio, F. Deep ultraviolet plasmon resonance in aluminum nanoparticle arrays. *ACS Nano* **2013**, *7*, 5834−5841.

(6) Martin, J.; Proust, J.; Gerard, D.; Plain, J. Localized surface plasmon resonances in the ultraviolet from large scale nanostructured aluminum films. *Opt. Mater. Express* **2013**, *3*, 954−959.

(7) Ayas, S.; Topal, A. E.; Cupallari, A.; Guner, H.; Bakan, G.; Dana, A. Exploiting Native Al_2O_3 for Multispectral Aluminum Plasmonics. *ACS Photonics* **2014**, *1*, 1313−1321.

(8) Bisio, F.; Proietti Zaccaria, R.; Moroni, R.; Maidecchi, G.; Alabastri, A.; Gonella, G.; Giglia, A.; Andolfi, L.; Nannarone, S.; Mattera, L.; Canepa, M. Pushing the high-energy limit of plasmonics. *ACS Nano* **2014**, *8*, 9239−9247.

(9) Knight, M. W.; King, N. S.; Liu, L.; Everitt, H. O.; Nordlander, P.; Halas, N. J. Aluminum for plasmonics. *ACS Nano* **2014**, *8*, 834−840.

(10) Norek, M.; Wlodarski, M.; Stepniowski, W. J. Tailoring of UV/violet plasmonic properties in Ag, and Cu coated Al concaves arrays. *Appl. Surf. Sci.* **2014**, *314*, 807−814.

(11) Liu, H.-W.; Lin, F.-C.; Lin, S.-W.; Wu, J.-Y.; Chou, B.-T.; Lai, K.-J.; Lin, S.-D.; Huang, J.-S. Single-Crystalline Aluminum Nanostructures on a Semiconducting GaAs Substrate for Ultraviolet to Near-Infrared Plasmonics. *ACS Nano* **2015**, *9*, 3875−3886.

(12) Martin, J.; Plain, J. Fabrication of aluminium nanostructures for plasmonics. *J. Phys. D: Appl. Phys.* **2015**, *48*, 48.

DOI: 10.1021/acsphotonics.5b00751
ACS Photonics 2016, 3, 796−805

(13) McPeak, K. M.; Jayanti, S. V.; Kress, S. J. P.; Meyer, S.; Iotti, S.; Rossinelli, A.; Norris, D. J. Plasmonic films can easily be better: Rules and recipes. *ACS Photonics* **2015**, *2*, 326−333.
(14) Lecarme, O.; Sun, Q.; Ueno, K.; Misawa, H. Robust and Versatile Light Absorption at Near-Infrared Wavelengths by Plasmonic Aluminum Nanorods. *ACS Photonics* **2014**, *1*, 538−546.
(15) Ramadurgam, S.; Lin, T.-G.; Yang, C. Aluminum plasmonics for enhanced visible light absorption and high efficiency water splitting in core-multishell nanowire photoelectrodes with ultrathin hematite shells. *Nano Lett.* **2014**, *14*, 4517−4522.
(16) Ramadurgam, S.; Chen, Y. Aluminum and copper plasmonics for enhancing internal quantum efficiency of core-shell and core-multishell nanowire photoelectrodes. *Proc. SPIE* **2014**, 91610J.
(17) Abdulrahman, R. B.; Cansizoglu, H.; Cansizoglu, M. F.; Herzog, J. B.; Karabacak, T. Enhanced light trapping and plasmonic properties of aluminum nanorods fabricated by glancing angle deposition. *J. Vac. Sci. Technol., A* **2015**, *33*, 041501.
(18) Kai, L.; Suhua, J.; Dengxin, J.; Xie, Z.; Nan, Z.; Haomin, S.; Yun, X.; Qiaoqiang, G. Super Absorbing Ultraviolet Metasurface. *IEEE Photonics Technol. Lett.* **2015**, *27*, 1539−1542.
(19) Lee, M.; Kim, J. U.; Lee, K. J.; Ahn, S.; Shin, Y.-B.; Shin, J.; Park, C. B. Aluminum Nanoarrays for Plasmon-Enhanced Light Harvesting. *ACS Nano* **2015**, *9*, 6206−6213.
(20) Tittl, A.; Michel, A.-K. U.; Schaferling, M.; Yin, X.; Gholipour, B.; Cui, L.; Wuttig, M.; Taubner, T.; Neubrech, F.; Giessen, H. A Switchable Mid-Infrared Plasmonic Perfect Absorber with Multispectral Thermal Imaging Capability. *Adv. Mater.* **2015**, *27*, 4597−4603.
(21) Sigle, D. O.; Perkins, E.; Baumberg, J. J.; Mahajan, S. Reproducible deep-UV SERRS on aluminum nanovoids. *J. Phys. Chem. Lett.* **2013**, *4*, 1449−1452.
(22) Norek, M.; Wlodarski, M.; Matysik, P. UV plasmonic-based sensing properties of aluminum nanoconcave arrays. *Curr. Appl. Phys.* **2014**, *14*, 1514−1520.
(23) Golmohammadi, S.; Ahmadivand, A. Fano Resonances in Compositional Clusters of Aluminum Nanodisks at the UV Spectrum: a Route to Design Efficient and Precise Biochemical Sensors. *Plasmonics* **2014**, *9*, 1447−56.
(24) Barrios, C. A.; Canalejas-Tejero, V.; Herranz, S.; Moreno-Bondi, M. C.; Avella-Oliver, M.; Puchades, R.; Maquieira, A. Aluminum Nanohole Arrays Fabricated on Polycarbonate for Compact Disc-Based Label-Free Optical Biosensing. *Plasmonics* **2014**, *9*, 645−9.
(25) Zheng, B. Y.; Wang, Y.; Nordlander, P.; Halas, N. J. Color-selective and CMOS-compatible photodetection based on aluminum plasmonics. *Adv. Mater.* **2014**, *26*, 6318−6323.
(26) Ren, F.-F.; Ang, K.-W.; Ye, J.; Yu, M.; Lo, G.-Q.; Kwong, D.-L. Split bull's eye shaped aluminum antenna for plasmon-enhanced nanometer scale germanium photodetector. *Nano Lett.* **2011**, *11*, 1289−1293.
(27) Tan, S. J.; Zhang, L.; Zhu, D.; Goh, X. M.; Wang, Y. M.; Kumar, K.; Qiu, C.-W.; Yang, J. K. W. Plasmonic color palettes for photorealistic printing with aluminum nanostructures. *Nano Lett.* **2014**, *14*, 4023−4029.
(28) Shrestha, V. R.; Lee, S.-S.; Kim, E.-S.; Choi, D.-Y. Aluminum plasmonics based highly transmissive polarization-independent subtractive color filters exploiting a nanopatch array. *Nano Lett.* **2014**, *14*, 6672−6678.
(29) Huang, Y.-W.; Chen, W. T.; Tsai, W.-Y.; Wu, P. C.; Wang, C.-M.; Sun, G.; Tsai, D. P. Aluminum plasmonic multicolor meta-Hologram. *Nano Lett.* **2015**, *15*, 3122−3127.
(30) Malhat, H. A.; Eltresy, N. A.; Zainud-Deen, S. H.; Awadalla, K. H. Reflectarray nano-dielectric resonator antenna using Different metals. *Appl. Comput. Electrom.* **2015**, *30*, 967−974.
(31) Ma, Y.-Q.; Shao, J.-H.; Zhang, Y.-F.; Lu, B.-R.; Zhang, S.-C.; Sun, Y.; Qu, X.-P.; Chen, Y.-F. Design and fabrication of structural color by local surface plasmonic meta-molecules. *Chin. Phys. B* **2015**, *24*.08070210.1088/1674-1056/24/8/080702
(32) Eizner, E.; Avayu, O.; Ditcovski, R.; Ellenbogen, T. Aluminum Nanoantenna Complexes for Strong Coupling between Excitons and Localized Surface Plasmons. *Nano Lett.* **2015**, *15*, 6215−6221.
(33) Cheng, L.; Huang, L.; Li, X.; Wu, J.; Zhang, Y.; Wang, J.; Cheng, L.; Liu, Y.; Feng, X.; Zhang, W.; Cai, Y. UV plasmonic resonance of aluminum shallow pit arrays. *J. Phys. Chem. C* **2015**, *119*, 14304−14311.
(34) Zhu, J.; Li, J.-J.; Zhao, J.-W. Tuning the plasmon band number of aluminum nanorod within the ultraviolet-visible region by gold coating. *Phys. Plasmas* **2014**, *21*, 112108.
(35) Ross, M. B.; Schatz, G. C. Aluminum and indium plasmonic nanoantennas in the ultraviolet. *J. Phys. Chem. C* **2014**, *118*, 12506−12514.
(36) Schwab, P. M.; Moosmann, C.; Wissert, M. D.; Schmidt, E. W. G.; Ilin, K. S.; Siegel, M.; Lemmer, U.; Eisler, H.-J. Linear and nonlinear optical characterization of aluminum nanoantennas. *Nano Lett.* **2013**, *13*, 1535−1540.
(37) Saito, Y.; Honda, M.; Watanabe, K.; Taguchi, A.; Yujian, S.; Kawata, S. Design of Aluminum Nanostructures for DUV Plasmonics: Blue Shifts in Plasmon Resonance Wavelength by Height Control. *Nippon Kinzoku Gakkaishi* **2013**, *77*, 27−31.
(38) Knight, M. W.; Liu, L.; Wang, Y.; Brown, L.; Mukherjee, S.; King, N. S.; Everitt, H. O.; Nordlander, P.; Halas, N. J. Aluminum plasmonic nanoantennas. *Nano Lett.* **2012**, *12*, 6000−6004.
(39) Zoric, I.; Zach, M.; Kasemo, B.; Langhammer, C. Gold, platinum, and aluminum nanodisk plasmons: Material independence, subradiance, and damping mechanisms. *ACS Nano* **2011**, *5*, 2535−2546.
(40) Langhammer, C.; Schwind, M.; Kasemo, B.; Zoric, I. Localized surface plasmon resonances in aluminum nanodisks. *Nano Lett.* **2008**, *8*, 1461−1471.
(41) Chu, Y.; Crozier, K. B. Experimental study of the interaction between localized and propagating surface plasmons. *Opt. Lett.* **2009**, *34*, 244−246.
(42) Oates, T. W. H.; Dastmalchi, B.; Isic, G.; Tollabimazraehno, S.; Helgert, C.; Pertsch, T.; Kley, E.-B.; Verschuuren, M. A.; Bergmair, I.; Hingerl, K.; Hinrichs, K. Oblique incidence ellipsometric characterization and the substrate dependence of visible frequency fishnet metamaterials. *Opt. Express* **2012**, *20*, 11166−11177.
(43) Brakstad, T.; Kildemo, M.; Ghadyani, Z.; Simonsen, I. Dispersion of polarization coupling, localized and collective plasmon modes in a metallic photonic crystal mapped by Mueller Matrix Ellipsometry. *Opt. Express* **2015**, *23*, 22800−22815.
(44) Oates, T. W. H.; Wormeester, H.; Arwin, H. Characterization of plasmonic effects in thin films and metamaterials using spectroscopic ellipsometry. *Prog. Surf. Sci.* **2011**, *86*, 328−376.
(45) Thackray, B. D.; Thomas, P. A.; Auton, G. H.; Rodriguez, F. J.; Marshall, O. P.; Kravets, V. G.; Grigorenko, A. N. Super-Narrow, Extremely High Quality Collective Plasmon Resonances at Telecom Wavelengths and Their Application in a Hybrid Graphene-Plasmonic Modulator. *Nano Lett.* **2015**, *15*, 3519−3523.
(46) Kravets, V. G.; Schedin, F.; Pisano, G.; Thackray, B.; Thomas, P. A.; Grigorenko, A. N. Nanoparticle arrays: From magnetic response to coupled plasmon resonances. *Phys. Rev. B: Condens. Matter Mater. Phys.* **2014**, *90*, 125445.
(47) Kravets, V. G.; Schedin, F.; Grigorenko, A. N. Extremely Narrow Plasmon Resonances Based on Diffraction Coupling of Localized Plasmons in Arrays of Metallic Nanoparticles. *Phys. Rev. Lett.* **2008**, *101*, 087403.
(48) Tittl, A.; Harats, M. G.; Walter, R.; Yin, X.; Schäferling, M.; Liu, N.; Rapaport, R.; Giessen, H. Quantitative Angle-Resolved Small-Spot Reflectance Measurements on Plasmonic Perfect Absorbers: Impedance Matching and Disorder Effects. *ACS Nano* **2014**, *8*, 10885−10892.
(49) Lodewijks, K.; Van Roy, W.; Borghs, G.; Lagae, L.; Van Dorpe, P. Boosting the Figure-Of-Merit of LSPR-Based Refractive Index Sensing by Phase-Sensitive Measurements. *Nano Lett.* **2012**, *12*, 1655−1659.

DOI: 10.1021/acsphotonics.5b00751
ACS Photonics 2016, 3, 796−805

(50) Aull, B. F. Silicon Geiger-mode avalanche photodiode arrays for photon-starved imaging. *Proc. SPIE* **2015**, 94920M.
(51) Schuette, D. R.; Reich, R. K.; Prigozhin, I.; Burke, B. E.; Johnson, R. New CCD imagers for adaptive optics wavefront sensors. *Proc. SPIE* **2014**, 91485O.
(52) Quintanilha, R.; Thony, P.; Henry, D.; Hazart, J. 3D features analysis using spectroscopic scatterometry. *Proc. SPIE* **2004**, *5375*, 456−67.
(53) Lodewijks, K.; Ryken, J.; Van Roy, W.; Borghs, G.; Lagae, L.; Van Dorpe, P. Tuning the Fano Resonance Between Localized and Propagating Surface Plasmon Resonances for Refractive Index Sensing Applications. *Plasmonics* **2013**, *8*, 1379−1385.
(54) Liu, N.; Mesch, M.; Weiss, T.; Hentschel, M.; Giessen, H. Infrared Perfect Absorber and Its Application As Plasmonic Sensor. *Nano Lett.* **2010**, *10*, 2342−2348.
(55) Liberman, V.; Adato, R.; Mertiri, A.; Yanik, A. A.; Kai, C.; Jeys, T. H.; Erramilli, S.; Altug, H. Angle-and polarization-dependent collective excitation of plasmonic nanoarrays for surface enhanced infrared spectroscopy. *Opt. Express* **2011**, *19*, 11202−12.
(56) Jellison, G. E.; Modine, F. A. Two-modulator generalized ellipsometry: theory. *Appl. Opt.* **1997**, *36*, 8190−8198.
(57) Walsh, G. F.; Forestiere, C.; Dal Negro, L. Plasmon-enhanced depolarization of reflected light from arrays of nanoparticle dimers. *Opt. Express* **2011**, *19*, 21081−21090.
(58) Bischoff, J. Improved diffraction computation with a hybrid C-RCWA-method. *Proc. SPIE* **2009**, 72723Y.
(59) Pond, J.; Kleckner, T.; Paddon, P.; Reid, A. Emerging trends in photonics modeling. *Proc. SPIE* **2006**, 612306−1.
(60) Grigorescu, A. E.; Hagen, C. W. Resists for sub-20-nm electron beam lithography with a focus on HSQ: state of the art. *Nanotechnology* **2009**, *20*, 292001.

DOI: 10.1021/acsphotonics.5b00751
ACS Photonics 2016, 3, 796−805